Sandwich-like CoMoP2 /MoP heterostructures coupling N, P co-doped carbon nanosheets as advanced anodes for high-performance lithium-ion batteries

Yiming Zhang

Shandong University

Liyuan Liu

Yantai University

Lanling Zhao

Shandong University

Chuanxin Hou (✉ chuanxin210@ytu.edu.cn)

Yantai University

Meina Huang

Taiyuan University of Science and Technology

Hassan Algadi

Najran University

Deyuan Li

Shandong University

Qing Xia

Shandong University

Jun Wang

Shandong University

Zhaorui Zhou

Shandong University

Xue Han

Shandong University

Yuxin Long

Shandong University

Yebing Li

Shandong University

Zidong Zhang

Shandong University

Yao Liu

Shandong University

Research Article

Abstract

Transition-metal phosphides as ideal anodes have been attracted a large number of interests due to their excellent performance for lithium-ion batteries. Nevertheless, $CoMoP_2$ materials were rarely reported as lithium-ion battery anode materials. Thereupon, to excavate their ability in LIBs, a sandwich-like architecture was employed as anode material, in which heterostructured $CoMoP_2$ and MoP nanoparticles were coated on N, P co-doped carbon matrix. Notably, doped carbon micro-lamellated sheets could not only allow boosted lithium-ion and electron transport, but also alleviate the volume changes of active material to sustain anode integrity during the discharge/charge processes. More importantly, the combination of $CoMoP_2$ and MoP nanoparticles could synergically strengthen the electrochemical activities of the anodes, and their built-in heterojunction facilitated the reaction kinetics on their interfaces. This research may offer a rational design on both heterostructure and doping engineering of future anodes for lithium-ion batteries.

1. Introduction

From the creation of Leyden jar to here various batteries, the unceasing evolution of energy storage system was a witness for the entire human modern civilization [1−3]. Owing to relatively stable cycle performance, high energy and operating voltage, sufficient range of use, safety and no memory effect, lithium-ion batteries (LIBs) realized extensive commercialization, which has already occupied the market of cars, mobile phones, laptops and most energy equipments [4−6]. It is evident that carbon as current commercial anode material, however, allows only one lithium-ion intercalated in six carbon atoms, and this could result in battery performance instability as a result of the volume expansion during lithium-ion insertion/extraction processes and inferior electrical conductivity, apparently hindering its electrochemical performance. Therefore, a quite low theoretical capacity of about 372 mAh g^{-1} was delivered, which is far away from the increasing pressure of fuel crisis and the emerging demand of future applications [7−9]. Such as it is, by the way of loading other active materials with rational architecture design, the carbon-based materials are expected to exhibit extraordinarily electrochemical performance in LIBs to address the aforementioned issues.

Because of their high theoretical capacities (500−1800 mAh g^{-1}), low polarization, comparatively low intercalation potentials *vs*. Li/Li$^+$ [10−12], numerous research efforts have been devoted to transition metal phosphides (TMPs) as anode materials for LIBs in recent years. To be honest, they could react completely with lithium ions via conversion reaction formula of $M_xP_y + 3yLi^+ + 3ye^- \leftrightarrow yLi_3P + xM^0$ during the discharge process, and it is obvious that one P atom could offer three positions for lithium-ion combination, which delivers a much higher specific capacity than that of carbon anode [13]. In addition, as a result of their electrochemical nature, TMPs typically exhibit triangular prism structure, where their metal atoms occupy in the apex positions and phosphorus atoms take the inner spaces of triangular prism [14], and this unique structure is believed to provide more active sites to improve electrochemical properties of TMP anodes. Although such a lot of merits the TMPs feature, two major shortcomings

restrict the practical application of TMP materials in LIBs. One is their inferior intrinsic electrical conductivity, resulting in a poor kinetics in the electrochemical reactions. Another is the volume changes in the charging/discharging processes, leading to severe pulverization and exfoliation of the active material within limited cycles. Decorating TMPs onto a carbon-based matrix is an effective way to deal with these matters, mainly because carbon matrix could relieve the volume changes and shorten the pathway of lithium-ion transition during shuttling. For instance, Wang *et al.* found that FeP could ameliorate the ionic conductivity and alleviate the volume changes in the processes of ion insertion and desertion, benefiting from the fact that Fe-P distance is larger than that of the lithium-ion diameter, and their hollow FeP@carbon nanocomposite encapsulating in graphene could provide more active sites, thus delivering excellent electrochemistry performance in both lithium-ion and sodium-ion batteries [12]. Except for this, it is evident that fruit of research on metal phosphides have also been conducted in power source fields, including Ni_2P immobilized on reduced graphene oxide [15], hollow carbon nanosheet encapsulated Cu_2P [16], CoP@C intertwined with N-doped carbon nanotubes [17], MoP/Mo_2C@C [18]. Interestingly, metal-rich TMPs with the formula of M_xP_y (x/y ≥ 1) normally display a character of metal materials, because of the existence of strong intensive M-M interactions [19]. On the contrary, with regard to phosphorus rich TMPs (x/y ≤ 1), most of their bonds are P-P or M-P. The more P atoms exist, the easier the P atoms gather together, leading to inferior properties in electrical conductivity and poor material stability [20]. It is worth noting that unitary TMPs can only offer single anionic active sites, while binary TMPs could provide more active sites to remarkably activate the lithium-ion insertion/extraction processes. Moreover, metal atoms in binary TMPs tend to form a triangular structure in an ordered way, and the center positions accommodate P atoms, which endows TMPs abundant electronic transmission channels [21] and good accommodated ability of lithium ions [22]. As an example of binary phosphides, Chen *et al.* reported that the Co substitution for Fe in FeP could resulted in increased density of states near Fermi level, significantly improving the intrinsic electrochemical activity of Co-Fe-P composite [23].

Among binary TMPs, $CoMoP_2$ and CoMoP have been intensively studied in hydrogen evolution reaction(HER) [24–28], oxygen evolution reaction(OER) [27] and oxygen reduction reaction(ORR) [22]. To the best of our knowledge, they have not been functioned as anode materials for LIBs up to now, and such binary TMP materials, honestly, could enable desired atom distribution of Co, Mo and P, which is expected to deliver an impressive effect for enhancing LIB performance.

Recently, heterostructures have been attracted a lot of attention in the research fields of photocatalysis [29], hydrogen evolution reaction (HER) [30] and water splitting [31], *etc.* It has been widely proved that with the distinct band gaps compounded in different components, the differences in Fermi energy levels combined together could build up an equilibrium of equal Fermi energy levels [32], thereby generating a space charge region, which could accelerate the charge transport and the interface reaction kinetics [33–35]. Enlightened by the unique architecture construction with different materials via physical and chemical combinations, heterostructures are desired to perfect the electrochemical properties for LIBs.

Herein, sandwich-like $CoMoP_2/MoP$ heterostructures coupling N, P co-doped carbon nanosheets ($CoMoP_2$-MoP@NPC) composites were successfully prepared through the process of solution evaporation and calcined treatment with regulating the addition contents of urea. It is believed that the NPC matrix with a multi-layered micro-/nano-architecture could not only supply a highly conductive network for facilitated transformation of lithium ions and electrons, but also promote the effective penetration of electrolyte and aid in easing the volume changes of the active $CoMoP_2/MoP$ heterostructures during cycling, beneficial for realizing their full electrochemical activities for lithium-ion storage.

2. Experimental Section

2.1. Synthetic procedures

200 mg of glucose, different amount of urea, 131 mL H▢PO▢, 275 mg of $Co(NO_3)_2 \cdot 6H_2O$ and 170 mg of $(NH_4)_6Mo_7O_{24}$ were first dispersed into 40 mL deionized water under vigorously stirring. Afterwards, the solutions were then dried in an oven at 80°C until all the solvent evaporated. Finally, the purple resultant was transferred into a tube furnace and heated in argon flow at 900°C for 2 hours with a ramp of 3°C minute^{-1}. After cooling down to room temperature, $CoMoP_2/MoP$@NPC composites were achieved, which are denoted as CMP@PC, CMP-2@NPC and CMP-4@NPC, with the urea addition amounts were 0, 2 and 4g, respectively. NPC was also fabricated as the same preparation route without employing $Co(NO_3)_2 \cdot 6H_2O$ and $(NH_4)_6Mo_7O_{24}$. The synthesis digital photos could be seen in Fig. S1.

2.2. Physical characterizations

The crystalline and phase structures of as-prepared samples were studied by X-ray diffraction (XRD, Rigaku D/Max-r B) with monochromatic Cu-Kα (λ = 1.5418 Å) line as the radiation source. The sample morphologies were inspected using field emission scanning electron microscope (FESEM, SU-70) and transmission electron microscope (TEM, JSM-7800F), and element information was collected by energy dispersive X-ray spectrometer (EDX) with an accelerating voltage of 20 kV equipped on the FESEM. The sample components were characterized by Raman spectroscopy (LabRam HR Evolution) with a 532 nm excitation laser. X-ray photoelectron spectroscopy (XPS, ESCALAB 250XI) was performed to analyze the surface chemical environment and composition, and all the XPS spectra were calibrated by C 1s = 284.8 eV. ASAP 2020 Micrometritics analyzer was utilized to research the N_2 adsorption/desorption characteristics. The mass ratio of Co/Mo was acquired through the inductively coupled plasma (ICP, Alilent 5110).

2.3. Electrochemical measurements

To test the electrochemical performance, a slurry consisting of 20 wt% Super P as the conductive agent, 10 wt % polyvinylidene fluoride (PVDF) as the binder and 70 wt% active materials were dispersed in N-methylpyrrolidone as the solvent. It was then homogeneously bladed on the copper foil and sent into a vacuum oven at 120°C overnight. Using these as-prepared anodes, CR2032 cells were assembled with a

Li disk as the counter and reference electrode in an argon-filled glovebox. The electrolyte composed of 1 M $LiPF_6$ in ethylene carbonate (EC) and diethyl carbonate (DEC) with a volume ratio of 1/1. The electrochemical performance of Li-ion cells was tested on a LANHE CT2001A battery tester at room temperature with the cutoff voltage between 0.01 and 3 V. Cyclic voltammetry (CV) and electrochemical impedance spectroscopy (EIS) data were recorded by using an electrochemical workstation (PARSTAT 2273).

3. Results And Discussion

As depicted in Fig. 1, the synthetic process of $CoMoP_2$-MoP@NPC composites was performed via a simple and effective route. Specifically, glucose, urea, H▨PO▨, $Co(NO_3)_2·6H_2O$ and $(NH_4)_6Mo_7O_{24}$ were added in deionized water under continuous stirring to form a reaction solution. After evaporating the solvent, the resultant was transferred into tube furnace for annealing activation, and composite material could be successively achieved.

FESEM observation of precursors were conducted, as shown in Fig. S2, and it could be seen that the morphology of NPC precursor seems like a cheese. With the increase of urea addition contents, precursors of CMP@PC, CMP-2@NPC, CMP-4@NPC presented apparent porous composition with more particles.

It was observed that NPC exhibit a lamellated structure in Fig. 2a, and CMP-2@NPC show a sandwich structure fully loaded with nanoparticles insides in Fig. 2b. Similar structure of CMP-4@NPC could be seen in Fig. S3, inferring that the NPC could play a vital role in homogenizing distribution of nanoparticles, and as for CMP@PC, the nanoparticles formed uneven clusters. As depicted in Fig. 2c, the TEM image indicates that these nanoparticles uniformly distributed throughout the layered nanosheets, HRTEM results were also recorded and shown in Fig. 2d. It could be clearly seen that the interplanar distances of two contiguous lattice fringes labeled by the orange and blue squares are 0.210 and 0.232 nm, corresponding to the (101) planes of the $CoMoP_2$ and (103) planes of the MoP, respectively, and interplanar distances of 0.334 nm are attributed to (002) planes of the graphitic matrix. These results turn out the existence of the heterostructures containing $CoMoP_2$ and MoP nanoparticles loaded on the carbon sheets. The selected area electron diffraction (SAED) pattern of the CMP-2@NPC is shown in Fig. 2e, demonstrating the diffraction rings matched well with lattice planes of (103) and (104) for $CoMoP_2$, (101) for MoP and (002) for graphitic matrix, respectively. The elemental mapping images were collected and presented in Fig. 2f-2k, manifesting the uniform distribution of Co, Mo N and P elements on the composite material. In order to learn the proportion of different ingredients in CMP-2@NPC, EDX measurement was performed, and the relative data was provided in Fig. S4. It is calculated that the mass ratio of $CoMoP_2$/MoP is 23.97/34.52, and the carbon matrix accounts for 41.51 wt% of the total composite material. According to the ICP result in Table. S1, the mass ratio of Co/Mo is 37.68/62.32, and it was deduced that the mass ratio of $CoMoP_2$/MoP is 1.52/1, which is close to EDX result.

Depicted in Fig. 3a, XRD patterns exhibit the crystalline structures of different samples. XRD pattern of the NPC shows a wide peak alone at about 26°, accorded with the (002) planes of graphitic material. Notably, with the change of urea contents, three samples display different compositions. Specifically, the phases of CMP@PC, CMP-2@NPC and CMP-4@NPC were identified with CoMoP-MoP, $CoMoP_2$-MoP and $CoMoP_2$, respectively, and all these peaks could be indexed by $CoMoP_2$ (JCPDS, No. 33−0428), CoMoP (JCPDS, No. 32−0299), MoP (JCPDS, No. 24−0771). XRD results of NPC, CMP-2@NPC and CMP-4@NPC precursors in Fig. S5 demonstrate that their main crystal phase is urea, and the precursor of CMP@PC appears a wide peak, owing to the presence of urea.
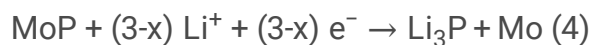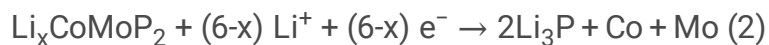
To investigate the degree of defects and graphitization on carbon matrix, Raman spectra of as-synthesized samples were employed, as shown in Fig. 3b. Two characteristic peaks could be seen at about 1346 and 1590 cm^{-1}, assigned to the D band and the G band, respectively, verifying carbon materials existed in these composites. As it is well known that the D band is associated with the disorders and defects in the graphene, caused by the point defects like nitrogen, phosphorus doping, displacements and distortions in the crystal faces, while the G band is related to the in-plane stretching vibration of sp^2-bonded carbon [36]. Consequently, the intensity ratio of the D band and the G band (I_D/I_G) reveals the degree of defects and disorders on the carbon matrix. It was traced that I_D/I_G of NPC, CMP@PC, CMP-2@NPC, CMP-4@NPC are 0.765, 0.639, 0.932 and 0.849 respectively, and the largest I_D/I_G value of CMP-2@NPC illustrate the formation of more active sites and defects on the carbon matrix, which could improve its electrochemical performance in a certain degree.

The specific surface area and pore size distribution of CMP-2@NPC was tested through the Brunauer-Emmett-Teller (BET) N_2 isothermal absorption-desorption measurement. As can be seen in Fig. 3c, the isotherm curve is corresponding to type H3 hysteresis loop in the P/P_0 range of 0.4-1.0, which shows a saturated adsorption platform and demonstrates the formation of uniform mesopores. It is calculated that the specific surface area of CMP-2@NPC is 75.368 $m^2 \, g^{-1}$, and the pore volume is 0.069 $cm^3 \, g^{-1}$. The pore size distribution curve analyzed by the BJH method inserted in Fig. 3c suggests a sharp peak located within 3−10 nm. This unique structure with sandwiched nanoparticles in the multilayered N, P co-doped carbon nanosheets is deem as a perfect accommodation to ease the volume expansion of CMP-2@NPC material during the lithiation/delithiation processes, shortening the lithium-ion transition distances and advancing the battery reversibility.

XPS measurement of CMP-2@NPC was conducted to investigate the surface elemental chemical compositions and the bonding configurations. The survey spectra in Fig. 3d overview the elements existing in CMP-2@NPC, and based on which, the N and C weight ratio on the NPC matrix could be roughly estimated to be 6.97%. The weight ratio of doped P and C can be affirmed to 3.43% according to the high-resolution XPS spectra of C 1s in Fig. 3e, and the peaks at binding energies of 284.8, 285.8 and 289.6 eV are matched well with C = C, C-N and C-P signals, implying the co-doped nature with N and P on carbon matrix [22]. As shown in high-resolution XPS spectra of Co 2p in Fig. 3f, doublets of Co $2p_{3/2}$ at 779.1 and 782 eV are ascribed to the Co-P and Co-O bonds, respectively, with a satellite peak located at

786.6 eV, and two peaks located at 794 and 798.3 eV are assigned to the Co $2p_{1/2}$ with a satellite peak at 803.1 eV [37−39]. In the Mo 3d region in Fig. 3g, two peaks seated at 229.2 and 231.5 eV indicate the Mo-P bond, turning out the intense incorporative interaction between Mo and P atoms. Moreover,peaks at 228.3, 232.6, 232.9, and 236 eV are indexed to Mo^{4+} and Mo^{6+} signals, mainly because of the surface oxidation of MoP originated from high surface energy [40−42]. As presented in P 2p region in Fig. 3h, the P-C bond settled at 133.7 eV as evidence, interpreting that P atoms successfully inserted in the carbon matrix. The peaks at binding energies at 130.1 and 131.2 eV could be assigned to P $2p_{3/2}$ and P $2p_{1/2}$ signals, and the P-O bond located at 134.3 could be attributed to phosphorus oxide species [24, 43−45]. It could also be found that the information of N atoms doped on the carbon matrix was offered in the high-resolution N1s spectrum in Fig. 3i. Concretely speaking, a distinct peak could be found at 398.9 eV, corresponding to N-C bond, and small peaks could be found at 397.9 and 400.6 eV, related to pyrrolic N and pyridinic N signals, respectively [22, 45, 46].

To elucidate the reactions at different potentials, CV curves of CMP-2@NPC anode was recorded within 0.01 to 3 V at 0.2 mV $s^{−1}$, as provided in Fig. 4a. It is clear that the negative peak centered at about 0.55 V in the initial cycle is distinguished from those after three cycles, and the differences is ascribed to the formation of solid electrolyte interface (SEI) films on the anode. The reaction routes were proposed as follows [13, 47, 48]:

$$CoMoP_2 + xLi^+ + xe^- \rightarrow Li_xCoMoP_2 \text{ (1)}$$

$$Li_xCoMoP_2 + (6\text{-}x) \, Li^+ + (6\text{-}x) \, e^- \rightarrow 2Li_3P + Co + Mo \text{ (2)}$$

$$MoP + xLi^+ + xe^- \rightarrow Li_xMoP \text{ (3)}$$

$$MoP + (3\text{-}x) \, Li^+ + (3\text{-}x) \, e^- \rightarrow Li_3P + Mo \text{ (4)}$$

An oxidation peak raised at about 1.25 V in the first anodic sweep, which could be assigned to the transformation from Li_3P to $CoMoP_2$ and MoP. In the follow cycles, the SEI layer peak disappeared, and a series of redox pairs located at 0.65 and 1.28 V appeared, which can be attributed to the reversible phase transition of Li_xCoMoP_2 and Li_xMoP in the lithium-ion insertion and disembedding processes. Additionally, the subsequent cycles display a similar characterization in the oxidation and reduction reactions, and the peaks overlapped and their positions almost unchanged, indicating an excellent reversible behavior and excellent stability.

Rate performance of the CMP-2@NPC anode for LIBs was researched, as given in Fig. 4b. It is revealed that at current densities of 100, 200, 400, 800 and 1500 mA $g^{−1}$, its specific capacities are 581, 524, 470, 407 and 360 mAh $g^{−1}$, respectively. Even at a high current density of 2000 mA $g^{−1}$, the corresponding reversible specific capacity still remained 344 mAh $g^{−1}$, and this specific capacity retention is 59.2% relative to that at 100 mA $g^{−1}$. When the current density returned back to 100 mA $g^{−1}$, the specific capacity recovered to 626 mAh $g^{−1}$, even higher than that of the initial cycles. This highly reversible

specific capacity was stable in the following cycles, resulting in favorable retention capability of CMP-2@NPC anode.

Cycling stability of different anodes were measured. As shown in Fig. 4d, the initial discharge/charge specific capacities of CMP-4@NPC, CMP-2@NPC, CMP@PC and NPC anodes at 100 mA g^{-1} are 692/433, 1001/680, 764/453 and 1108/584 mAh g^{-1}, with the corresponding initial coulombic efficiency (ICE) of 62.6%, 67.9%, 59.3% and 52.7%, respectively. The specific capacities of corresponding composite anodes increased to 556.6, 693.2, 621.7 mAh g^{-1} after 150 cycles, revealing the superior capacity of the CMP-2@NPC anode. Figure 4c shows the selected discharge-charge profiles of CMP-2@NPC anode at 100 mAh g^{-1} within a cutoff voltage window of 0.01-3 V. It could be seen that the initial discharge/charge specific capacities are 1001.9/620.4 mAh g^{-1}, revealing the ICE of approximately 62%. The relatively low ICE can be mainly ascribed to the formation of the SEI films, consistent with the CV results. From the second cycle, the ICE raised and reached almost 93%, and this value could be further increase through the process of activation [17, 49, 50]. After 150 cycles, the specific capacity of discharge/charge process come to 693/657 mAh g^{-1}, which is higher than that of the first several cycles.

Even at 500 mA g^{-1} in Fig. 4e and Fig. S6, the CMP-4@NPC, CMP-2@NPC and CMP@PC anodes delivered the retentive specific capacity of 607.6, 689.3 and 514.3 mAh g^{-1} after 700 cycles, respectively. Besides, the cycling performance of CMP-2@NPC anode at 1 A g^{-1} was also included in Fig. S7, and it still exhibited about 530 mAh g^{-1} after 900cycles with the similar phenomenon occurred. This enhanced specific capacity was mainly as a result of the activation processes, which has been widely reported in other conversion-type and transition metal phosphide anodes for LIBs [17, 47, 51].

In order to excavate the transport kinetics of the CMP-2@NPC anode, its EIS data were provided with the equivalent circuit model inserted. Fig. S8 shows the EIS profiles of CMP-2@NPC anode monitored after 200, 400 and 600 cycles. Normally, the semicircle seated at middle-frequency region is assigned to the charge transfer resistance (R_c) with the double-layer capacitance (C_d). It is worth noting that R_c after 200, 400 and 600 cycles gradually become smaller. These results are well consisted with the discharge/charge profiles showing an obvious specific capacity increase, and this phenomenon could also be attributed to the activation treatment, which greatly improved the cycling performance [17]

4. Conclusion

In summary, CoMoP$_2$-MoP@NPC composites were successfully synthesized through a facile strategy of directly annealing the evaporated reactants, in which the heterostructures consist of CoMoP$_2$ and MoP nanoparticles were sandwiched in NPC nanosheets. Thanks to the unique architecture, the transportation acceleration of lithium ions and electrons was realized, and the volume changes during the lithiation duration was released. Therefore, the composite anode delivered a surpassed specific capacity of 693.2

mAh g^{-1} after 150 cycles at 100 mA g^{-1}, and similar electrochemical performance occurred even at 500 mA g^{-1}, attributed to the activation processes during cycling. These superior electrochemical properties demonstrate CoMoP$_2$-MoP@NPC composites can be served as efficient anode materials for LIBs, with the expectation for other transition metal phosphides applied in various energy-related fields.

Declarations

Competing Interest

Authors' Contributions

Funding' section in the Declarations

References

1. Che G, Lakshmi B, Fisher E, Martin C (1998) Carbon nanotubule membranes for electrochemical energy storage and production. Nature 393:346–349
2. Meng Y (2020) Introduction: beyond Li-Ion battery chemistry. Chem Rev 120:6327–6327
3. Sun J, Mu Q, Kimura H, Murugadoss V, He M, Du W, Hou C (2022) Oxidative degradation of phenols and substituted phenols in the water and atmosphere: a review. Adv Compos Hybrid Mater. https://doi.org/10.1007/s42114-022-00435-0
4. Zhu G, Guo R, Luo W, Liu H, Jiang W, Dou S, Yang J (2021) Boron doping-induced interconnected assembly approach for mesoporous silicon oxycarbide architecture. Natl Sci Rev 8:naww152
5. Chu S, Cui Y, Liu N (2017) The path towards sustainable energy. Nat Mater 16:16–22
6. Dang C, Mu Q, Xie X, Sun X, Yang X, Zhang Y, Maganti S, Huang M, Jiang Q, Seok I, Du W, Hou C, (2022) Recent progress in cathode catalyst for nonaqueous lithium oxygen batteries: a review, https://doi.org/10.1007/s42114-022-00500-8

7. He C, Wu S, Zhao N, Shi C, Liu E, Li J (2013) Carbon-encapsulated Fe_3O_4 nanoparticles as a high-rate lithium ion battery anode material. ACS Nano 7:4459−4469

8. Wang H, Cui L, Yang Y, Casalongue H, Robinson J, Liang Y, Cui Y, Dai H (2010) Mn_3O_4-graphene hybrid as a high-capacity anode material for lithium ion batteries. J Am Chem Soc 132:13978−13980

9. Li M, Ma Y, Chen J, Lawrence R, Luo W, Sacchi M, Jiang W, Yang J (2021) Residual chlorine induced cationic active species on a porous copper electrocatalyst for highly stable electrochemical CO_2 Reduction to C_{2+}. Angew Chem Int Ed 60:11487−11493

10. Bichat M, Politova T, Pfeiffer H, Tancret F, Monconduit L, Pascal J, Brousse T, Favier F (2004) Cu_3P as anode material for lithium ion battery: powder morphology and electrochemical performances. J Power Sources 136:80−87

11. Cabana J, Monconduit L, Larcher D, Palacin M (2010) Beyond intercalation-based Li-ion batteries: the state of the art and challenges of electrode materials reacting through conversion reactions. Adv Mater 22:E170-E192

12. Wang X, Chen K, Wang G, Liu X, Wang H (2017) Rational design of three-dimensional graphene encapsulated with hollow FeP@Carbon nanocomposite as outstanding anode material for lithium ion and sodium ion batteries. ACS Nano 11:11602−11616

13. Shi Y, Li M, Yu Y, Zhang B (2020) Recent advances in nanostructured transition metal phosphides: synthesis and energy-related applications. Energy Environ Sci 13:4564−4582

14. Oyama S, Gott T, Zhao H, Lee Y (2009) Transition metal phosphide hydroprocessing catalysts: a review. Catal Today 143:94−107

15. Cai G, Wu Z, Luo T, Zhong Y, Guo X, Zhang Z, Wang X, Zhong B (2020) 3D hierarchical rose-like Ni_2P@rGO assembled from interconnected nanoflakes as anode for lithium ion batteries. RSC Adv 10:3936−3945

16. Chen S, Wu F, Shen L, Huang Y, Sinha S, Srot V, van Aken P, Maier J, Yu Y (2018) Cross-linking hollow carbon sheet encapsulated CuP_2 nanocomposites for high energy density sodium-ion batteries. ACS Nano 12:7018−7027

17. Guo K, Xi B, Wei R, Li H, Feng J, Xiong S (2020) Hierarchical microcables constructed by CoP@C⊂Carbon framework intertwined with carbon nanotubes for efficient lithium storage. Adv Energy Mater 10:1902913

18. Zhang L, Li S, Tan H, Khan S, Ma Y, Zang H, Wang Y, Li Y (2017) MoP/Mo_2C@C: a new combination of electrocatalysts for highly efficient hydrogen evolution over the entire pH range. ACS Appl Mater Interfaces 9:16270−16279

19. Hou C, Hou Y, Fan Y, Zhai Y, Wang Y, Sun Z, Fan R, Dang F, Wang J (2018) Oxygen vacancy derived local build-in electric field in mesoporous hollow Co_3O_4 microspheres promotes high-performance Li-ion batteries. J Mater Chem A 6:6967−6976

20. Chen J, Whitmire K (2018) A structural survey of the binary transition metal phosphides and arsenides of the d-block elements. Coord Chem Rev 355:271–327

21. El Sharkawy H, Sayed D, Dhmees A, Aboushahba R, Allam N (2020) Facile synthesis of nanostructured binary Ni-Cu phosphides as advanced battery materials for asymmetric electrochemical supercapacitors. ACS Appl Energy Mater 3:9305–9314

22. Xu H, Zhao L, Liu X, Li D, Xia Q, Cao X, Wang J, Zhang W, Wang H, Zhang J (2021) $CoMoP_2$ nanoparticles anchored on N, P doped carbon nanosheets for high-performance lithium-oxygen batteries. FlatChem 25:100221

23. Chen J, Liu J, Xie J, Ye H, Fu X, Sun R, Wong C (2019) Co-Fe-P nanotubes electrocatalysts derived from metal-organic frameworks for efficient hydrogen evolution reaction under wide pH range. Nano Energy 56:225–233

24. Huang X, Xu X, Luan X, Cheng D (2020) CoP nanowires coupled with CoMoP nanosheets as a highly efficient cooperative catalyst for hydrogen evolution reaction. Nano Energy 68:104332

25. Zhang T, Wang Y, Yuan J, Fang K, Wang A (2022) Heterostructured CoP·CoMoP nanocages as advanced electrocatalysts for efficient hydrogen evolution over a wide pH range. J Colloid Interface Sci 615:465–474

26. Chen M, Liu Z, Zhang X, Zhong A, Qin W, Liu W, Liu Y (2021) In-situ phosphatizing of cobalt-molybdenum nanosheet arrays on self-supporting rGO/CNTs film as efficient electrocatalysts for hydrogen evolution reaction. Chem Eng J 422:130355

27. Zhang Y, Shao Q, Long S, Huang X (2018) Cobalt-molybdenum nanosheet arrays as highly efficient and stable earth-abundant electrocatalysts for overall water splitting. Nano Energy 45:448–455

28. Ma Y, Wu C, Feng X, Tan H, Yan L, Liu Y, Kang Z, Wang E, Li Y (2017) Highly efficient hydrogen evolution from seawater by a low-cost and stable CoMoP@C electrocatalyst superior to Pt/C. Energy Environ Sci 10:788–798

29. Ong W, Shak K (2020) 2D/2D heterostructured photocatalysts: an emerging platform for artificial photosynthesis. Sol RRL 4:2000132

30. Zhao G, Rui K, Dou S, Sun W (2018) Heterostructures for electrochemical hydrogen evolution reaction: a review. Adv Funct Mater 28:1803291

31. Zhao D, Wang Y, Dong C, Huang Y, Chen J, Xue F, Shen S, Guo L (2021) Boron-doped nitrogen-deficient carbon nitride-based Z-scheme heterostructures for photocatalytic overall water splitting. Nat Energy 6:388–397

32. Xia Q, Zhao L, Zhang Z, Wang J, Li D, Han X, Zhou Z, Long Y, Dang F, Zhang Y, Chou S (2021) $MnCo_2S_4$-$CoS_{1.097}$ heterostructure nanotubes as high efficiency cathode catalysts for stable and long-life lithium-oxygen batteries under high current conditions. Adv Sci 8:2103302

33. Zheng Y, Zhou T, Zhang C, Mao J, Liu H, Guo Z (2016) Boosted charge transfer in SnS/SnO_2 heterostructures: toward high rate capability for sodium-ion batteries. Angew Chem Int Ed 55:3408–3413

34. Zhao C, Li Y, Zhang W, Zheng Y, Lou X, Yu B, Chen J, Chen Y, Liu M, Wang J (2020) Heterointerface engineering for enhancing the electrochemical performance of solid oxide cells. Energy Environ Sci 13:53–85

35. Ma Y, Xie X, Yang W, Yu Z, Sun X, Zhang Y, Yang X, Kimura H, Hou C, Guo Z, Du W (2021) Recent advances in transition metal oxides with different dimensions as electrodes for high-performance supercapacitors. Adv Compos Hybrid Mater 4:906–924

36. Wang J, Liu L, Chou S, Liub H, Wang J (2017) A 3D porous nitrogen-doped carbon-nanofiber-supported palladium composite as an efficient catalytic cathode for lithium-oxygen batteries. J Mater Chem A 5:1462–1471

37. Wang D, Zhang X, Zhang D, Shen Y, Wu Z (2016) Influence of Mo/P Ratio on CoMoP nanoparticles as highly efficient HER catalysts. Appl Catal A-Gen 511:11–15

38. Wei Z, Wang Z, Xu C, Fan G, Song X, Liu Y, Fan R (2022) Defect-induced insulator-metal transition and negative permittivity in $La_{1-x}Ba_xCoO_3$ perovskite structure. J Mater Sci Technol 112:77–84

39. Zhai Y, Yang W, Xie X, Sun X, Wang J, Yang X, Naik N, Kimura H, Du W, Guo Z, Hou C (2022) Co_3O_4 nanoparticle-dotted hierarchical-assembled carbon nanosheet framework catalysts with the formation/decomposition mechanisms of Li_2O_2 for smart lithium-oxygen batteries. Inorg Chem Front 9:1115–1124

40. Li G, Sun Y, Rao J, Wu J, Kumar A, Xu Q, Fu C, Liu E, Blake G, Werner P, Shao B, Liu K, Parkin S, Liu X, Fahlman M, Liou S, Auffermann G, Zhang J, Felser C, Feng X (2018) Carbon-tailored semimetal MoP as an efficient hydrogen evolution electrocatalyst in both alkaline and acid media. Adv Energy Mater 8:1801258

41. Chen T, Fu Y, Liao W, Zhang Y, Qian M, Dai H, Tong X, Yang Q (2021) Fabrication of cerium-doped CoMoP/MoP@C heterogeneous nanorods with high performance for overall water splitting. Energy Fuels 35:14169–14176

42. Hou C, Yang W, Xie X, Sun X, Wang J, Naik N, Pan D, Mai X, Guo Z, Dang F, Du W (2021) Agaric-like anodes of porous carbon decorated with MoO_2 nanoparticles for stable ultralong cycling lifespan and high-rate lithium/sodium storage. J Colloid Interface Sci 596:396–407

43. Lan K, Wang X, Yang H, Iqbal K, Zhu Y, Jiang P, Tang Y, Yang Y, Gao W, Li R (2018) Ultrafine MoP nanoparticles well embedded in carbon nanosheets as electrocatalyst with high active site density for hydrogen evolution. ChemElectroChem 5:2256–2262

44. Darband G, Aliofkhazraei M, Hyun S, Shanmugam S (2020) Pulse electrodeposition of a superhydrophilic and binder-free Ni-Fe-P nanostructure as highly active and durable electrocatalyst for both hydrogen and oxygen evolution reactions. ACS Appl Mater Interfaces 12:53719–53730

45. Qin Q, Jang H, Li P, Yuan B, Liu X, Cho J (2019) A tannic acid-derived N-, P-codoped carbon-supported iron-based nanocomposite as an advanced trifunctional electrocatalyst for the overall water splitting cells and zinc-air batteries. Adv Energy Mater 9:1803312

46. Xu H, Zhao L, Liu X, Huang Q, Wang Y, Hou C, Hou Y, Wang J, Dang F, Zhang J (2020) Metal-organic-framework derived core-shell N-doped carbon nanocages embedded with cobalt nanoparticles as

high-performance anode materials for lithium-ion batteries. Adv Funct Mater 30:2006188

47. Wang X, Sun P, Qin J, Wang J, Xiao Y, Cao M (2016) A three-dimensional porous MoP@C hybrid as a high-capacity, long-cycle life anode material for lithium-ion batteries. Nanoscale 8:10330–10338

48. Zhu P, Zhang Z, Zhao P, Zhang B, Cao X, Yu J, Cai J, Huang Y, Yang Z (2019) Rational design of intertwined carbon nanotubes threaded porous CoP@carbon nanocubes as anode with superior lithium storage. Carbon 142:269–277

49. Li X, Gu M, Hu S, Kennard R, Yan P, Chen X, Wang C, Sailor M, Zhang J, Liu J (2014) Mesoporous silicon sponge as an anti-pulverization structure for high-performance lithium-ion battery anodes. Nat Commun 5:4105

50. Ma Y, Ma Y, Bresser D, Ji Y, Geiger D, Kaiser U, Streb C, Varzi A, Passerini S (2018) Cobalt disulfide nanoparticles embedded in porous carbonaceous micro-polyhedrons interlinked by carbon nanotubes for superior lithium and sodium storage. ACS Nano 12:7220–7231

51. Choi Y, Choi W, Yoon W, Kim J (2022) Unveiling the genesis and effectiveness of negative fading in nanostructured iron oxide anode materials for lithium-ion batteries. ACS Nano 631–642
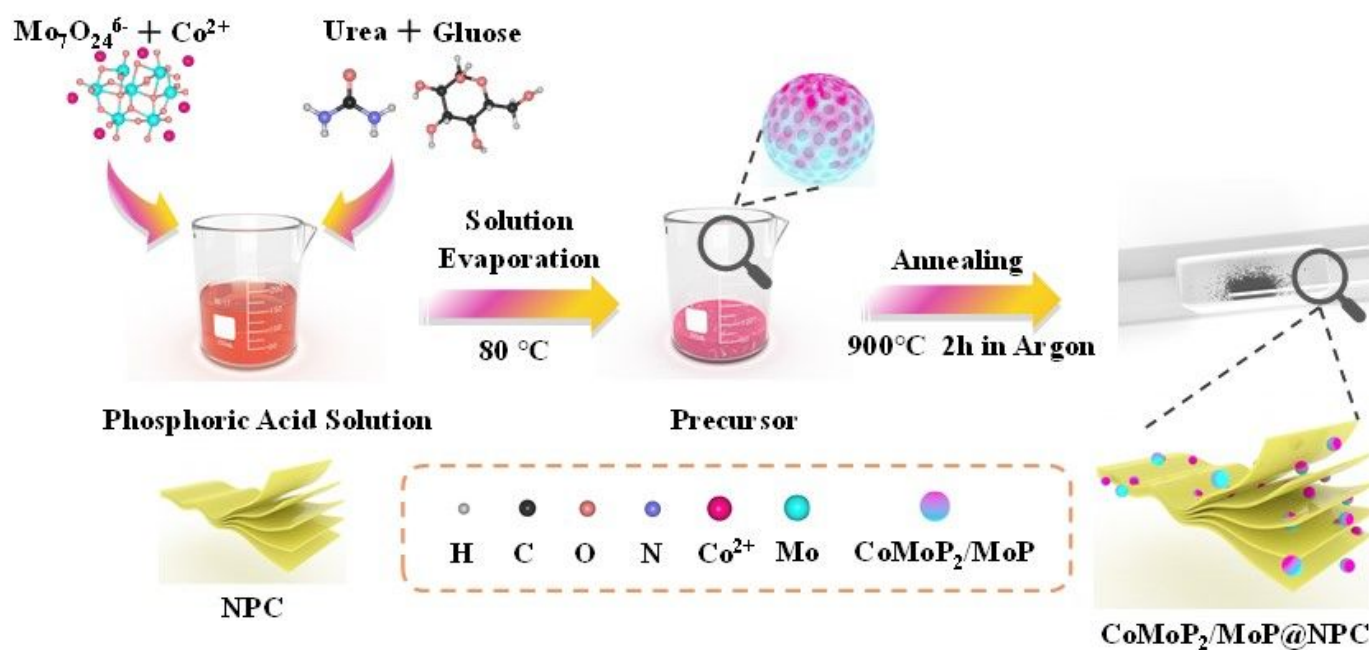
Figures

Figure 1

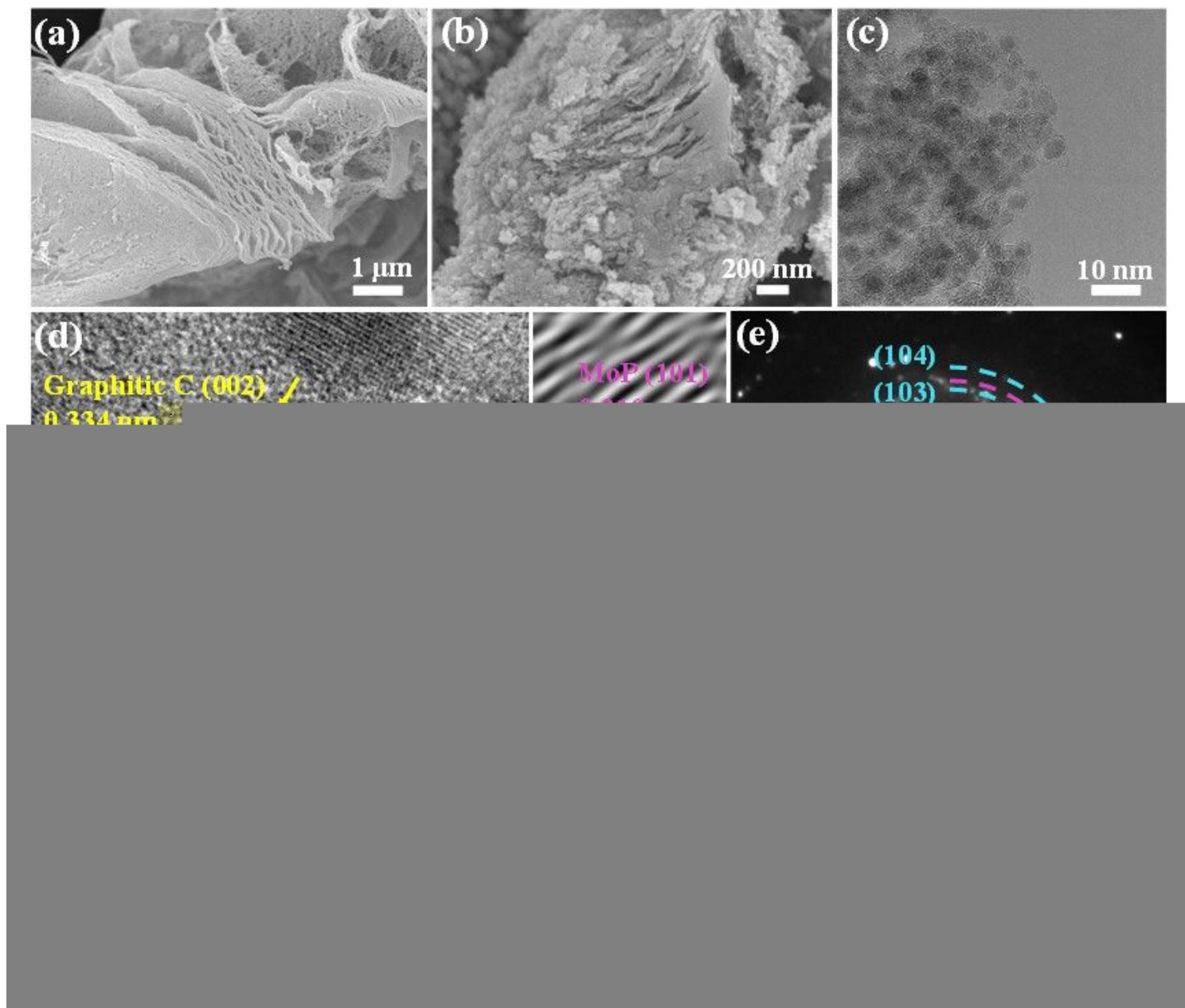Schematic illustration of synthesis of the sandwich-like CoMoP$_2$-MoP@NPC composites.

Figure 2

FESEM images of (a) NPC and (b) CMP-2@NPC; (c) TEM image, (d) HRTEM image with magnification of corresponding regions, (e) SAED pattern and (f-k) EDX-elemental mapping images of CMP-2@NPC.

Figure 3

(a) XRD patterns and (b) Raman spectra of different samples; (c) N_2 adsorption-desorption isotherm and pore size distribution, (d)XPS survey and (e-i) high-resolution XPS spectra of CMP-2@NPC.

Figure 4

(a) CV curves at 0.1 mV s^{-1}, (b) rate performance at 0.1-2 A g^{-1} and (e) cycling performance of CMP-2@NPC anodes at 500 mA g^{-1}; (d) cycling performance of different anodes at 100 mA g^{-1} with (c) selected charge-discharge profiles of CMP-2@NPC anode.
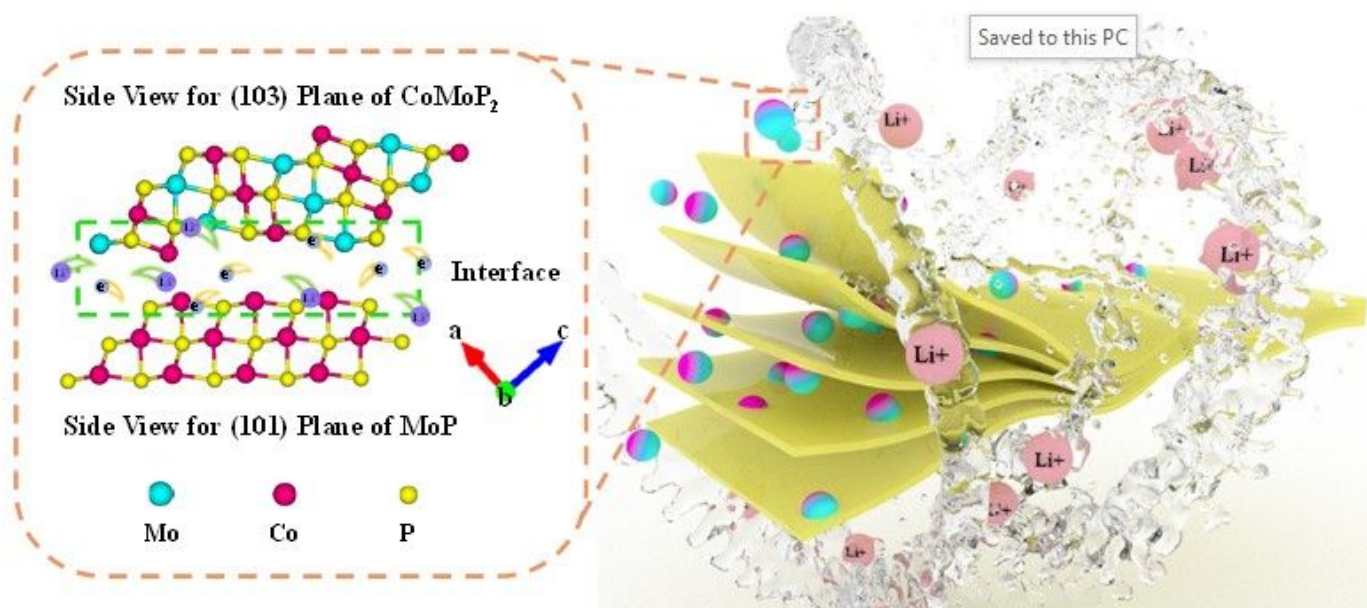

Figure 5

Proposed mechanism illustration of CMP-2@NPC anode for LIBs in charge and discharge processes.

Supplementary Files

This is a list of supplementary files associated with this preprint. Click to download.

- SupportingInformation.docx